Manchester Metropolitan University

e-space

Manchester Metropolitan University's Research Repository

Please cite the Published Version

Daghrah, M, Zhang, X, Wang, Z, Liu, Q, Jarman, P and Walker, D (2019) Flow and temperature distributions in a disc type winding-part I: Forced and directed cooling modes. Applied Thermal Engineering, 165. ISSN 1359-4311

DOI: https://doi.org/10.1016/j.applthermaleng.2019.114653

Publisher: Elsevier

Version: Published Version

Downloaded from: https://e-space.mmu.ac.uk/625848/

Usage rights: CC BY Creative Commons: Attribution 4.0

Additional Information: This is an Open Access article published in Applied Thermal Engineering published and copyright Elsevier.

Enquiries:
If you have questions about this document, contact openresearch@mmu.ac.uk. Please include the URL of the record in e-space. If you believe that your, or a third party's rights have been compromised through this document please see our Take Down policy (available from https://www.mmu.ac.uk/library/using-the-library/policies-and-guidelines)

Applied Thermal Engineering 165 (2020) 114653

Contents lists available at ScienceDirect

Applied Thermal Engineering

journal homepage: www.elsevier.com/locate/apthermeng

Research Paper

Flow and temperature distributions in a disc type winding-part I: Forced and directed cooling modes

Muhammad Daghrah[a], Xiang Zhang[a], Zhongdong Wang[a,*], Qiang Liu[a], Paul Jarman[a], David Walker[b]

[a] School of Electrical and Electronic Engineering, The University of Manchester, Manchester M13 9PL, UK
[b] Scottish Power, Glasgow, UK

HIGHLIGHTS

- Typical operational conditions for forced and directed cooled transformers were tested.
- The Reynolds number predominates liquid flow and temperature distributions.
- 3D flow and temperature distribution features were identified when reverse flows occur.
- Variation of hotspot factor with the Reynolds number is shown.

ARTICLE INFO

Keywords:
CFD
Disc-type winding
Dimensional analysis
PIV
Transformer

ABSTRACT

The thermal design of a power transformer determines its lifetime and loading capability, so correct modelling of liquid flow and temperature distributions in the winding is of vital importance. Existing standards and widely used simple calculation models can seriously under/overestimate winding hotspot temperatures under certain circumstances. In this paper, liquid flow and temperature distributions in a physical model representing a disc-type winding in a liquid forced and directed cooling mode are investigated experimentally using Particle Image Velocimetry (PIV) and a temperature measurement system and numerically using Computational Fluid Dynamics (CFD). Dimensional analysis is used to generalise the results into a form useful for design review. The operating conditions investigated include different liquid inlet velocities, inlet temperatures, power losses in individual disc segments, and the effect of alternative liquids. It is shown that hotspot temperature and position within the winding are a non-linear function of liquid inlet velocity, with stagnation and reverse flow demonstrated in both experiments and CFD models. Comparisons of liquid flow and temperature distributions between measurements and CFD simulation results show that 2D CFD results are representative when there are no reverse flows and 3D CFD simulations are needed when reverse flows occur. The results are presented first in dimensional forms to show the effect of each parameter, and then in non-dimensional forms to provide a generalised insight into transformer thermal design.

1. Introduction

Transformer utilization in terms of balancing lifetime with both long and short term loading depends critically on an accurate calculation of the hottest spot temperature under a range of load and ambient temperature conditions. The ageing rate of the cellulose based insulation paper increases exponentially with temperature, and this ageing is generally taken to determine the useful lifetime of the transformer [1]. Additionally, there is a temperature at which bubbles will form in the liquid-solid insulation system, which could trigger a transformer failure.

Liquid immersed power transformers represent the most common type in power networks with the liquid serving both as a dielectric and a coolant. The cooling relies on thermal convection from either a natural liquid circulation between the winding and the cooler/radiator by thermosiphon action or on forced liquid circulation using pumps. In

* Corresponding author.
E-mail addresses: MuhammadDaghrah@mimaterials.com (M. Daghrah), xiang.zhang@manchester.ac.uk (X. Zhang), zhongdong.wang@manchester.ac.uk (Z. Wang), qiang.liu@manchester.ac.uk (Q. Liu), paul.jarman@manchester.ac.uk (P. Jarman), David.Walker2@spenergynetworks.co.uk (D. Walker).

https://doi.org/10.1016/j.applthermaleng.2019.114653
Received 18 July 2019; Received in revised form 25 September 2019; Accepted 5 November 2019
Available online 20 November 2019
1359-4311/ © 2019 The Authors. Published by Elsevier Ltd. This is an open access article under the CC BY license (http://creativecommons.org/licenses/BY/4.0/).

Nomenclature

A	surface area of the pass inlet vertical duct (m^2)
c_p	specific heat (J/(kg·K))
c_{p1}	mineral oil specific heat (J/(kg·K))
c_{p2}	gas-to-liquid specific heat (J/(kg·K))
c_{p3}	synthetic ester specific heat (J/(kg·K))
D_h	hydraulic diameter (m)
k	thermal conductivity (W/(K·m))
k_1	mineral oil thermal conductivity (W/(K·m))
k_2	gas-to-liquid thermal conductivity (W/(K·m))
k_3	synthetic ester thermal conductivity (W/(K·m))
L	perimeter of the inlet vertical duct (m)
Pr	the Prandtl number
Re	the Reynolds number
T*	dimensionless temperature
T_{to}	top liquid temperature (K)
T_{aw}	average winding temperature (K)
T_{bo}	bottom liquid temperature (K)
u_m	winding pass inlet average velocity (m/s)
ρ	density of the liquid (kg/m^3)
ρ_1	mineral oil density (kg/m^3)
ρ_2	gas-to-liquid density (kg/m^3)
ρ_3	synthetic ester density (kg/m^3)
μ	dynamic viscosity (Pa·s)
μ_1	mineral oil dynamic viscosity (Pa·s)
μ_2	gas-to-liquid dynamic viscosity (Pa·s)
μ_3	synthetic ester dynamic viscosity (Pa·s)

many core-form disc-type power transformer designs, the liquid is directed through radial ducts in the cylindrical winding in a zig-zag fashion using blocking washers within cylinders forming axial ducts inside and outside the winding.

Liquid forced and directed cooled transformers, henceforth referred to as oil directed (OD) transformers, exhibit different thermal behaviour compared to liquid natural cooled transformers, henceforth referred to as oil natural (ON) transformers. This is because oil flow velocities and the relationship between that velocity and loading are different between OD and ON cooling modes [2].

Power transformer thermal performance in terms of average winding temperature rise, liquid temperature rise, and hotspot temperature rise in a steady state at rated load is the standard for transformer thermal design. Compliance with international standards and the purchaser's specification is partially validated by the temperature rise test during factory acceptance testing but measuring hotspot temperatures is complicated by needing to know in advance where the hotspot will be and the use of specifically introduced probes. Often hotspot temperatures are determined by a standard calculation based on thermal diagram that depends on estimated hotspot factor [1,3].

Dimensional analysis gives the hotspot factor a physical meaning—the highest dimensionless temperature, which for fixed geometry and power loss distribution is controlled by the Reynolds, Prandtl and Richardson numbers [4,5]. In addition, the geometric dimensions are reduced to the most important one—the ratio of horizontal duct height to vertical duct width, referred to as α in [6].

To model transformer thermal behaviour in a steady state, thermal-hydraulic network models employing relatively few nodes and branches have been developed since the 1980s [7,8]. Computational Fluid Dynamics (CFD) models share the same physical principles, i.e. conservation of mass, momentum and energy, as network models but solve the governing equations directly using numerical methods [5,6,9–11]. Network models are quick to compute and capable of dealing with the complete transformer cooling loop, while CFD models are more reliable and provide detailed results at the expense of a much higher computational requirement and are therefore normally used for the modelling of part of the cooling loop, e.g. the winding or the cooler/radiator.

Comparisons of liquid flow and temperature predictions between 2D CFD with 3D CFD reveal that 3D CFD has better accuracy but requires much more computational resources [11–13]. An improvement strategy for matching axisymmetric 2D CFD key results (top oil, average winding and hotspot temperatures) with their 3D counterparts was reported in [13].

Experimentally, liquid flow rates have been measured within various disc type winding models using different techniques such as Hot Wire Anemometry [14], Laser Doppler Velocimetry [15,16], and Particle Image Velocimetry (PIV) through the optical tracking of seeding particles [12,17,18].

In this paper, OD cooling modes are studied extensively using experimental and numerical tools with the aid of dimensional analysis to document the thermal behaviour, i.e. liquid flow and temperature distributions, under diverse and representative operating conditions. Big pictures of liquid flow and temperature distribution variation trends for different operating conditions and liquids used are presented to aid OD transformer thermal design review. A companion paper on ON cooling modes is followed as part II of the study. Section 2 presents the methodology for both theoretical and experimental investigations. Section 3 presents new experimental and numerical results in dimensional forms, showing the influences of key parameters along with comparisons between 2D and 3D CFD results with experimental measurements. Section 4 presents all these new results in their dimensionless forms for simplicity, insight and universal applicability, followed by conclusion in Section 5.

2. Methodology

2.1. Governing equations and dimensional analysis

Fluid flow and heat transfer in the winding cooling ducts are governed by the conservation laws for mass, momentum and energy. In OD cooling modes, the effect of the buoyancy force is negligible and therefore fluid flow can be decoupled from heat transfer [18]. The governing equations in nondimensional forms are given as follows, the detailed deduction of these equations is given in [4]:

$$\nabla^*\mathbf{u}^* = 0$$

$$(\mathbf{u}^*\cdot\nabla^*)\mathbf{u}^* = -\nabla^* p^* + \frac{1}{Re}\nabla^{*2}\mathbf{u}^*$$

$$\mathbf{u}^*\cdot(\nabla^* T^*) = \frac{1}{Re\cdot Pr}(\nabla^{*2} T^*)$$

where the del operator ∇^* incorporates a characteristic length D_h to make it dimensionless ($\nabla^* = D_h\nabla$), with the characteristic length chosen to be the hydraulic diameter of the pass inlet vertical duct, $D_h = 4A/L$. The coordinates are normalised against the hydraulic diameter, velocity normalised against winding pass inlet velocity and the pressure against twice the dynamic pressure at the winding pass inlet. The dimensionless temperature is defined as $T^* = \frac{T - T_{to}}{T_{aw} - (T_{to} + T_{bo})/2}$. The definition of dimensionless temperature takes the same format as in defining the hotspot factor. Therefore, the highest dimensionless temperature is the hotspot factor.

From the nondimensional governing equation sets, one can conclude that for a fixed winding geometry in OD cooling modes the dimensionless flow distribution or volumetric flow fraction distribution is dictated by the Reynolds number (Re) at the pass inlet;

$$Re = \frac{\rho u_m D_h}{\mu}$$

the dimensionless temperature distribution or the hotspot factor is

controlled by both Re and the Prandtl number (Pr).

$$Pr = \frac{\mu c_p}{k}$$

Previous CFD study showed that *Re* is much more influential than *Pr* for OD transformer cooling conditions [4].

2.2. Experimental setup

The experimental setup, as shown in Fig. 1, consists of a winding model, a radiator, a positive displacement flow meter with 0.5% reading accuracy, a centrifugal pump, and connecting pipework. The winding model was made of rectangular Aluminium plates with dimensions of 100 mm (depth) × 104 mm (horizontal/radial width) × 10 mm (vertical/axial height). The reason to simplify the winding model to rectangular shape is to facilitate manufacturing and flow distribution measuring processes. In addition, liquid flow and temperature distribution trends in rectangular models and fan-shaped models are the same, as shown by planar 2D and axisymmetric 2D CFD comparisons [4,6,18]. Each Aluminium plate was imbedded with two resistive cartridge heaters to inject power and imitate losses in the winding. In addition, each plate was imbedded with two K-type thermocouples at the entrance and exit sides of the horizontal duct to record temperatures with calibrated accuracy of ± 1 °C. 10 plates were placed horizontally in a 12 mm thick polycarbonate housing in such a way as to form 11 uniform horizontal ducts with a height of 4 mm, and 2 vertical ducts with a width of 10 mm. This structure was repeated to form a total of 3 passes. The passes were segregated by using 10 mm thick polycarbonate plates, referred to as washers as shown in Fig. 1. Since the winding model is symmetric about a vertical plane, only half of it is shown in Fig. 1.

In the winding model, plates are referenced sequentially from bottom to top as plate 1 to plate 30. Since liquid flow rates in the horizontal ducts were only measured in pass 3 (the top pass), the horizontal ducts in pass 3 are referred to as duct 1 at the bottom to duct 11 at the top. The top liquid temperature (T_{to}) used is the average of the measurements from 8 thermocouples distributed at the outlet of pass 3. The winding inlet liquid temperature (T_{in}) is the average of the measurements from the 3 thermocouples installed at the inlet of pass 1.

A PIV system with a precision of 0.1 mm/s was used to measure flow rates in the pass 3 horizontal cooling ducts. The PIV system consists of dual head laser sources, a camera, a synchronizer, and processing software. Seeding particles of silver coated hollow glass spheres with a diameter of 10–14 μm were doped in the cooling liquid. The PIV system functions as follows: the laser source fires two consecutive laser pulses with a predetermined time delay between them. Each laser pulse is passed through the laser sheet optics to create a laser sheet to illuminate the seeding particles. The synchronizer coordinates the camera with the laser source. During each laser pulse, the camera captures an image. By tracking the movements of seeding particles in captured image pairs, the software can extract and map out the velocity fields.

For the duct flow measurements, the camera was focused on a 20 mm length of the horizontal cooling ducts near the duct exit. The laser sheet was directed through the horizontal cooling duct in the direction of liquid flow and positioned 15 mm away from the front winding model wall facing to the camera. A detailed description of the PIV system used is given in [18,19]. The experimental setup design including a detailed description of the winding model, plate design, and instrumentation used is given in [18,20].

2.3. CFD simulations

CFD models for the winding model were built using commercial software COMSOL Multiphysics, in which the governing equations for mass, momentum and energy conservations were solved directly using finite element methods. Since the winding model was symmetric, only half of the winding was simulated.

For 3D CFD models, structured/mapped meshes were adopted for the fluid domain and the winding housing, as shown in Fig. 2. Quadrilaterals were inserted in the symmetry plane in the fluid domain to enable mapped mesh. 30 and 55 elements were used to discretise horizontal duct height and vertical duct width, respectively, and other parts were meshed with free triangles. The symmetry plane was first meshed and then swept to create 3D mesh with 75 elements present in the swept dimension. The mesh of 2D models had similar mesh pattern as the 3D symmetry plane mesh but with finer mesh (horizontal duct height 60 elements, vertical duct width 80 elements). The meshes were arranged in such a way that more layers present near the wall to capture hydraulic and thermal boundary layers. Mesh refinement studies were conducted to guarantee mesh independent results. The final numbers of elements for 3D and 2D models were 17,304,800 and 988,906 respectively. The workstation used for the simulation has 768 GB Ram and 2 Intel E6 CPUs. A typical 2D simulation requires tens of GB RAM and computation time of several hours, while a 3D simulation requires hundreds of GB RAM and computation time of several days.

The properties of the liquids used in CFD are set as functions of temperature, which are derived from measured data points from the liquid manufacturers, as shown below [21,22]:

$$\begin{cases} \rho_1 = -0.6568\times T + 1064 \\ \mu_1 = 7.863\times10^{-5}\times\exp(632.0/(T-176.0)) \\ k_1 = -7.837\times10^{-5}\times T + 0.1557 \\ c_{p1} = 3.950\times T + 560.2 \\ \rho_2 = -0.6455\times T + 995.5 \\ \mu_2 = 6.133\times10^{-5}\times\exp(749.8/(T-157.4)) \\ k_2 = -8.217\times10^{-5}\times T + 0.1674 \\ c_{p2} = 4.449\times T + 871.7 \\ \rho_3 = -0.7327\times T + 1185.1 \\ \mu_3 = 6.23883011\times10^{-5}\times\exp(914.1/(T-162.4)) \\ k_3 = -1.236\times10^{-4}\times T + 0.1817 \\ c_{p3} = 2.069\times T + 1287 \end{cases}$$

where ρ is for density, μ for dynamic viscosity, k for thermal conductivity, c_p for specific heat (all in SI units), the subscript 1 for a mineral oil (MO), 2 for a gas to liquid (GTL) oil, 3 for a synthetic ester

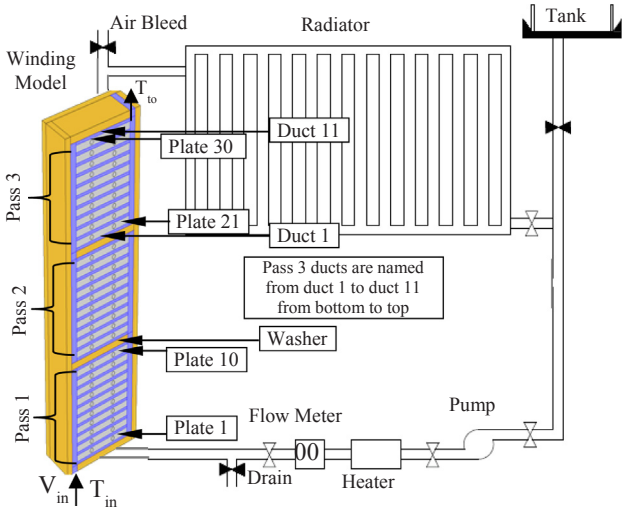

Fig. 1. Experimental setup with half of the winding model shown. The yellow part shows the transparent polycarbonate housing and washers, the blue parts for the liquid domain, the grey parts for the aluminium plate and the circles for the cartridge heaters. (For interpretation of the references to colour in this figure legend, the reader is referred to the web version of this article.)

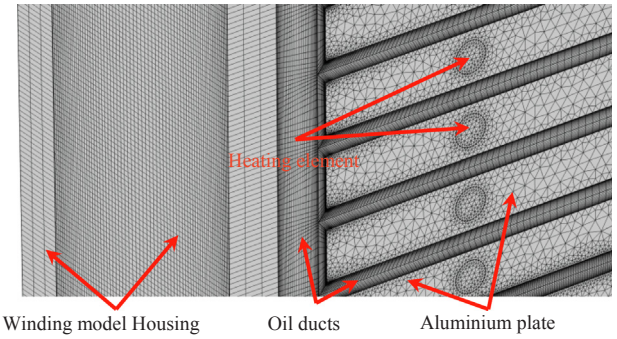

Fig. 2. Mesh for 3D CFD models. The symmetry plane was first meshed and then swept to create the 3D mesh.

(SE), T for temperature in Kelvin.

3. Results

Results in this section are divided into two subsections. Section 3.1 presents some of the representative experimental test results on liquid flow and temperature distributions in pass 3 for different operational conditions (total liquid flow rate, winding power loss and liquid inlet temperature) and different liquids. The liquid used is a mineral oil if not specified otherwise. The ambient temperature ranged from 22 to 24 °C. It was taken that a steady state was reached when the temperature change in 1 h was less than ± 1 °C. A steady state was reached in 3 h from the start of the test. The desired inlet temperature was obtained by slightly altering the external heater to counter any fluctuations in ambient temperature during the test such that the fluctuation of the inlet temperature was within ± 1 °C. Section 3.2 focuses on the comparisons between measurements and 2D and 3D CFD simulation results.

3.1. Experimental results

3.1.1. Pass inlet velocity (V_{in})

Tests were conducted under fixed uniform power losses in each plate of 50 W/plate which is equivalent to a plate average surface flux of 2010 W/m^2. This power loss corresponds to the resistive power loss with a current density of 4.85 A/mm^2 flowing through a copper plate of the winding model plate size at 75 °C. Pass 1 inlet temperature (T_{in}) was fixed at 60 °C.

The liquid flow and temperature results in pass 3 shown in Fig. 3 are of three different values of V_{in} 0.1 m/s, 0.2 m/s, and 0.3 m/s. In transformer design, the upper limit of liquid flow velocity in OD cooling modes is usually set to be 0.5 m/s to avoid the possibility of static electrification. In our test setup and geometric arrangement, however, liquid reverse flows start to occur at 0.3 m/s with representative liquid temperatures. Because reverse flows should be avoided in transformer design, we limited our test velocity to 0.3 m/s. For the present winding model, these velocities are equivalent to 6, 12, and 18 L/minute, respectively. Fig. 3 represents the liquid flow distribution, i.e. the measured average velocity in each radial cooling duct in pass 3, and the temperature distribution, i.e. the average plate temperatures (average of the two thermocouples in each plate) in pass 3 in the winding model. Some geometric deviations in the winding model caused a temperature "footprint" which is discussed in more detail in [23]. However, the focus here is on the effect of V_{in}. Higher V_{in} caused more uneven flow and temperature distributions. Under V_{in} = 0.3 m/s, a reverse flow was recorded in duct 1, causing a higher plate temperature than the counterpart under V_{in} = 0.2 m/s, as circled in Fig. 3. Thus, in contradiction to the conventional expectation, higher V_{in} does not always reduce the hotspot temperature, particularly when liquid stagnation or reverse flow occurs.

3.1.2. Power losses (P_{loss})

Tests were conducted under fixed T_{in} = 60 °C and V_{in} = 0.3 m/s with heat fluxes on the plate surface, P_{loss}, of 804 W/m^2, 1608 W/m^2 and 2814 W/m^2. Liquid flow and temperature distributions are shown in Fig. 4. Under the tested conditions, the effect of P_{loss} on the liquid flow distribution was negligible because the change of viscosity arising from the change in oil temperature rise was negligible. Higher P_{loss} directly increased the plate temperatures. From these results, it is concluded that in OD cooling mode conditions the thermal system has a negligible effect on the hydraulic system.

3.1.3. Pass 1 inlet liquid temperature (T_{in})

Tests were conducted with a fixed P_{loss} of 2010 W/m^2 and V_{in} of 0.3 m/s with T_{in} of 43 °C, 55 °C, and 65 °C at the inlet of pass 1. The test results are shown in Fig. 5. Higher T_{in} and the consequent higher *Re* caused a more uneven flow distribution evidenced by liquid stagnation at 55 °C and reverse flow at 65 °C in the bottom duct of the pass. Due to the stagnation and reverse flow, higher temperature gradients were observed at the bottom of pass 3 for cases with T_{in} being 55 °C and 65 °C than the case with T_{in} being 43 °C.

3.1.4. Transformer liquid type

Alternative liquids to mineral oil have been used to provide specific features, for example, higher purity, higher fire resistance, or better biodegradability. In this part, tests were conducted using three different liquids. A naphthenic hydrocarbon based mineral oil (MO), as used in the previous tests, a gas-to-liquid hydrocarbon-based transformer liquid (GTL), and a synthetic ester transformer liquid (SE). For each liquid the test was conducted with V_{in} = 0.2 m/s, P_{loss} = 2010 W/m^2, and T_{in} = 70 °C. The main difference between the thermal properties of the different liquids is in their individual viscosities. SE has a higher viscosity than GTL and MO, which have similar viscosities, resulting in lower *Re* for the SE at the same flow rate. Under the tested conditions, SE shows a more uniform liquid flow and temperature distributions than the other two liquids as shown in Fig. 6 at the expense of a higher pressure drop. The pressure drops over the winding are 278 Pa for SE, 198 Pa for MO and 180 Pa for GTL.

When V_{in} was increased to 0.27 m/s, MO and GTL both suffered from reverse flows at the bottom of the pass, while SE continued to cool normally. The differences in flow distribution result in the hotspot temperature of SE being 6 °C lower than MO and GTL under these conditions, as detailed in [24]. At lower inlet velocity and liquid temperature, *Re* would be lower for all the liquids and the hotspot temperature of SE is comparable (difference less than 1 °C) to the other

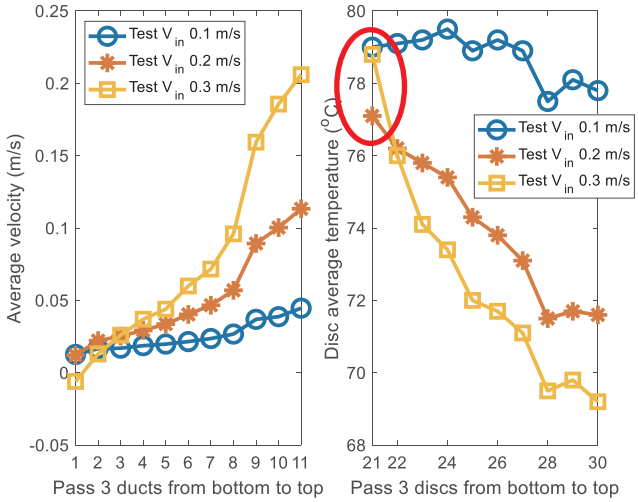

Fig. 3. Liquid flow and temperature distributions in pass 3 under varied inlet velocities and fixed T_{in} = 60 °C and P_{loss} = 2010 W/m^2.

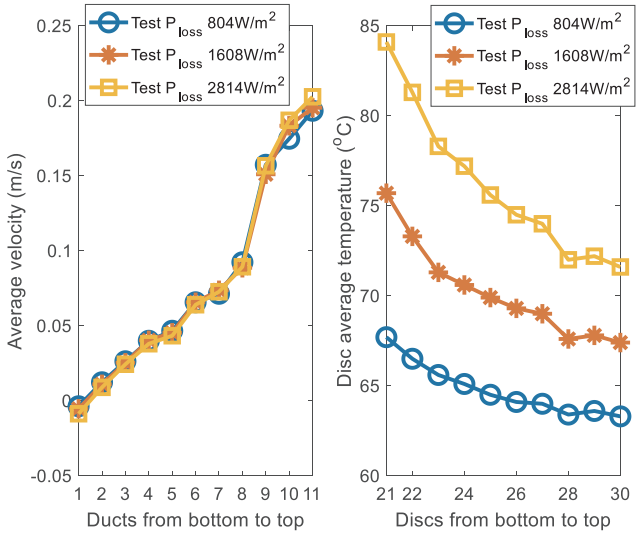

Fig. 4. Liquid flow and temperature distributions under varied power losses and fixed T_{in} = 60 °C and V_{in} = 0.3 m/s.

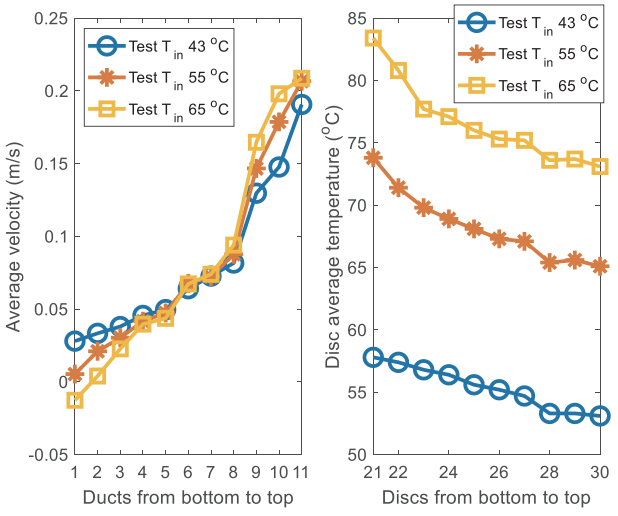

Fig. 5. Liquid flow and temperature distributions under varied pass inlet liquid temperatures with P_{loss} = 2010 W/m^2 and V_{in} = 0.3 m/s.

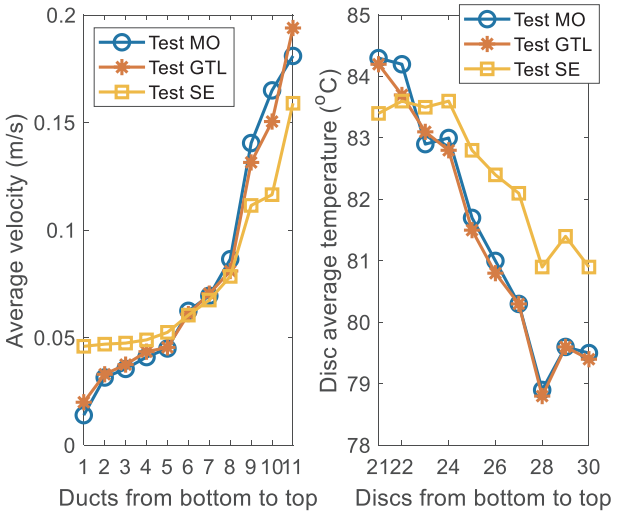

Fig. 6. Liquid flow and temperature distributions for different liquids with tests conducted under V_{in} = 0.2 m/s, P_{loss} = 2010 W/m^2, and T_{in} = 70 °C.

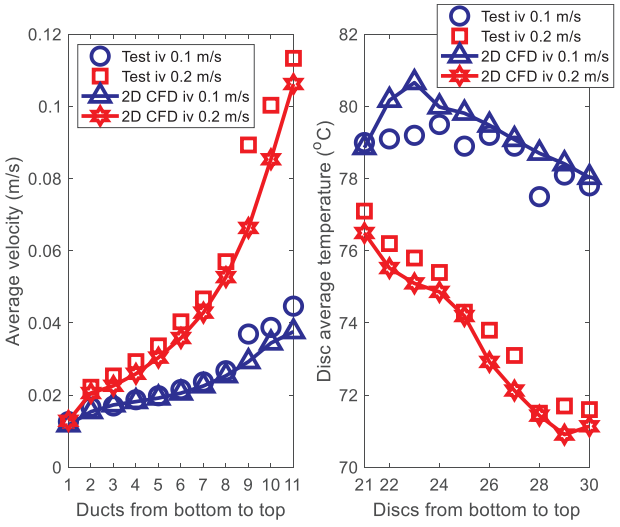

Fig. 7. Comparison between 2D CFD simulations and experimental measurements under two different pass inlet velocity of 0.1 m/s and 0.2 m/s and fixed P_{loss} = 2010 W/m^2 and T_{in} = 60 °C.

liquids.

3.2. Comparison with CFD results

3.2.1. Without liquid reverse flows

Results from planar 2D CFD simulations were compared with experimental measurements of liquid flow and temperature distributions in pass 3 for T_{in} = 60 °C, P_{loss} = 2010 W/m^2, and V_{in} of 0.1 m/s and 0.2 m/s, as shown in Fig. 7. In the CFD simulations, a heat transfer coefficient of 10 W/(K·m^2) was specified on the outer surface of the housing to account for free air convection and radiation to the environment. In these conditions no flow reversal or stagnation occurred and flow and temperature results from measurements and simulations are comparable, with the maximum temperature difference between measurements and simulations being less than 2 °C.

3.2.2. With liquid reverse flows

When V_{in} was increased to 0.3 m/s with T_{in} = 60 °C and P_{loss} = 2010 W/m^2, reverse flows started to occur at the bottom of the pass. The comparisons of flow and temperature distributions in pass 3 between measurements and 2D and 3D CFD simulations are shown in Fig. 8.

2D and 3D CFD simulations can both produce flow distributions that match the PIV measurements and predict the occurrence of reverse flows. However, the 2D CFD temperature prediction for the plate surrounded by a reverse flow was much higher (20.1 °C) than the measurement, while the 3D CFD counterpart was only 1.6 °C higher than the measurement. The comparison of 2D and 3D CFD temperature contours are shown in Fig. 9. 2D CFD does not have the third dimension and therefore cannot represent the practical liquid flow and heat transfer phenomena observed to occur also in the third dimension. The temperature prediction differences for disc 21 between 2D and 3D CFD simulations are due to convection in the bottom duct being important. As shown in the circled region in Fig. 10 from the 3D CFD simulation, the existence of a strong flow swirl close to the side wall of the duct entrance, which is also observed in experimental tests [19], allows convection in the bottom duct. Although the overall flow direction in duct 1 is reversed with average duct velocity being −0.0011 m/s (minus sign indicates flow reversal), the maximum velocity of the swirl is higher than 0.1 m/s, and this increases the heat transfer. The 2D and 3D model streamlines passing through the entrance to duct 1 for this condition excluding other streamlines are shown in Fig. 11. In the 2D

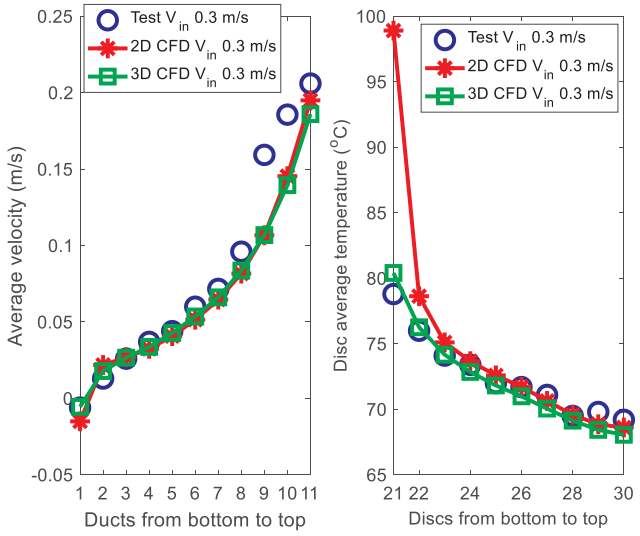

Fig. 8. Results comparison between experimental measurements and both 2D and 3D CFD simulations under the condition of V_{in} = 0.3 m/s, P_{loss} = 2010 W/m^2, and T_{in} = 60 °C.

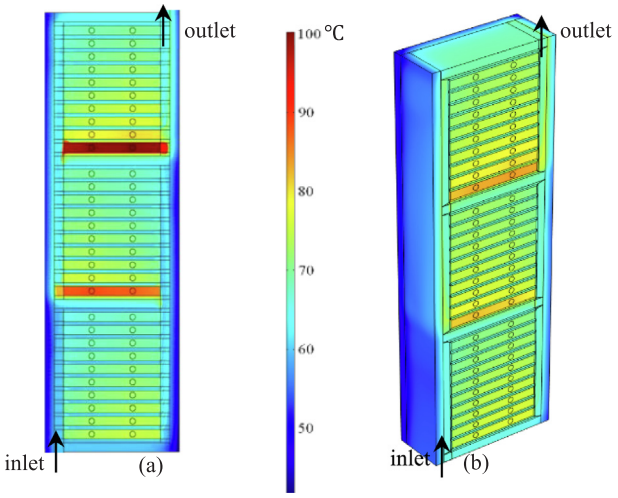

Fig. 9. 2D and 3D temperature contours under the condition of V_{in} = 0.3 m/s, P_{loss} = 2010 W/m^2, and T_{in} = 60 °C. 2D and 3D temperature contours share the same colour bar.

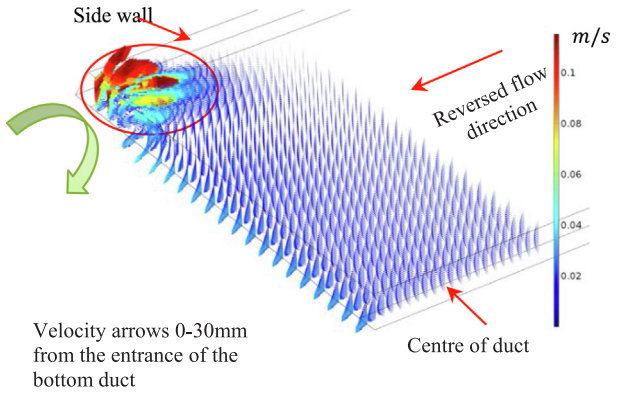

Fig. 10. Detailed view of duct 1 velocity arrows from a 3D CFD simulation when reverse flows occur under V_{in} = 0.3 m/s, P_{loss} = 2010 W/m^2, and T_{in} = 60 °C.

case it is notable that the flows exiting from the duct 1 entrance all enter into duct 2 and form a closed loop effectively eliminating

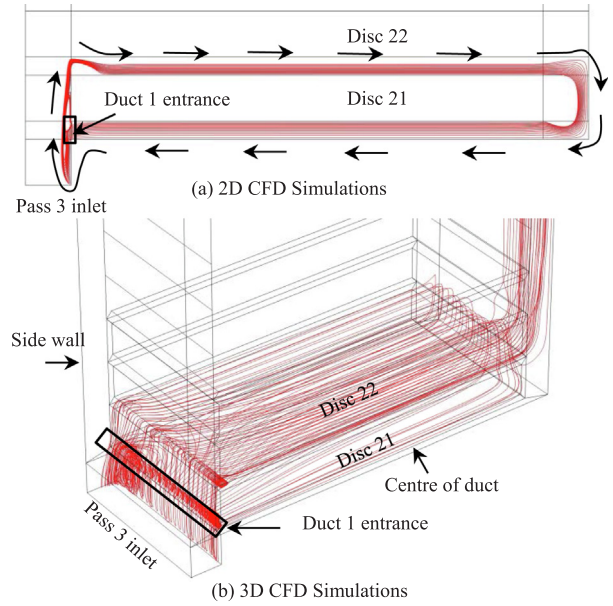

Fig. 11. Streamline representation of flow patterns in ducts with reverse flows in 2D and 3D CFD cases. The streamlines shown all originate from the entrance of duct 1 to trace out the ins and outs.

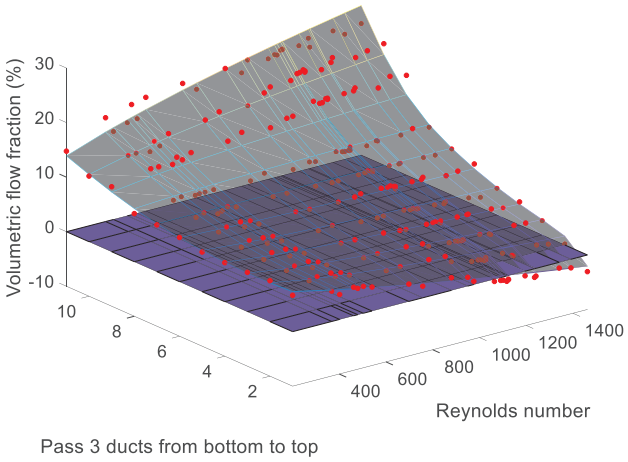

Fig. 12. Comparisons of flow fractions from PIV measurements and the correlation.

convection in the bottom duct. In the 3D case the third component of velocity allows part of the flow from duct 1 to go through duct 2 and escape the duct-1-duct-2 closed loop therefore enabling partial convection to other parts of the winding pass.

4. Dimensionless representation

4.1. Liquid flow fraction distribution

The liquid flow fraction distribution in the winding pass is controlled by *Re* at the pass inlet. 2D CFD parametric sweeps of *Re* in isothermal conditions were conducted and the results of liquid flow fraction in each duct were correlated with *Re* to form a predictive correlation equation set, for which the details are presented in [6,18].

The liquid flow fraction distributions from PIV measurements for all the inlet velocities, inlet temperatures, power losses and liquid types are shown in Fig. 12 as red dots. According to *Re* of each case the flow fraction in each duct can be predicted by the correlation. The predicted flow fraction distributions from the correlation equations are shown by

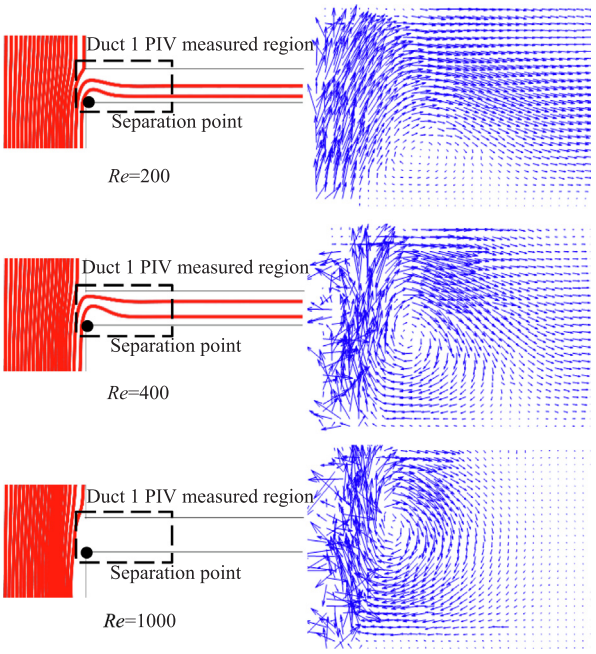

Fig. 13. Flow separation at the entrance of the bottom duct in relation to *Re*. Left column for 2D CFD streamline representation with all streamlines originated from the pass inlet and right column for corresponding PIV measurements at the entrance of the bottom duct (duct 1).

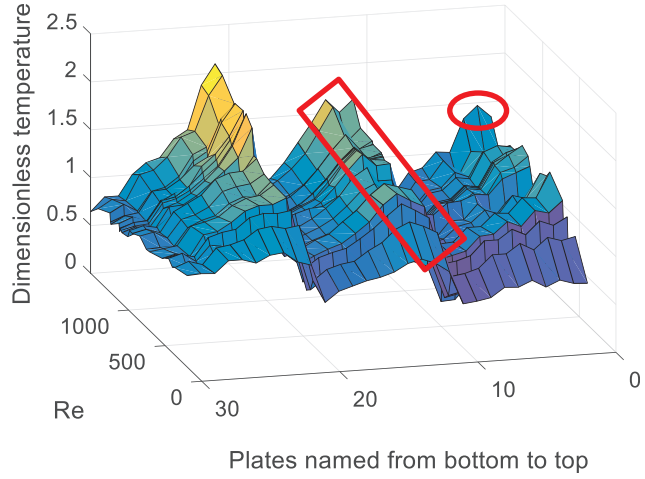

Fig. 14. Dimensionless plate maximum temperature distributions from all the OD tests.

the mesh in Fig. 12. A close match between the PIV measurements and the correlation is obtained with a mean error of 0.9% of the total flow rate and a standard deviation of 0.9%.

The flow distribution gets increasingly uneven with the increase of *Re* and reverse flows occur when *Re* is higher than approximately 1000. The flow distribution variation with *Re* is related to the flow separation at the entrance of the horizontal cooling duct when the flow is diverted from a vertical direction to a horizontal direction. As shown in Fig. 13 by the streamline representation from the 2D CFD simulations and the corresponding flow field measured by PIV at the entrance of duct 1, the separation causes flow recirculation in the separated zone i.e. the bottom part of the horizontal duct entrance and reduces the effective height of the horizontal duct. The separation is more pronounced at the bottom part of the pass and gets severer as *Re* increases and can eventually 'block' the duct entrance and initiate flow reversal.

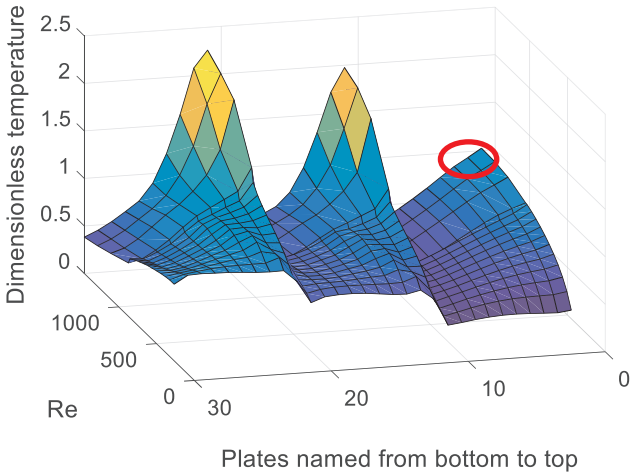

Fig. 15. Dimensionless plate maximum temperature distributions from 2D and 3D CFD simulations. The last 4 cases with high *Re* shown by the coarse mesh are from 3D CFD and the others with smaller *Re* shown by a finer mesh are from 2D CFD.

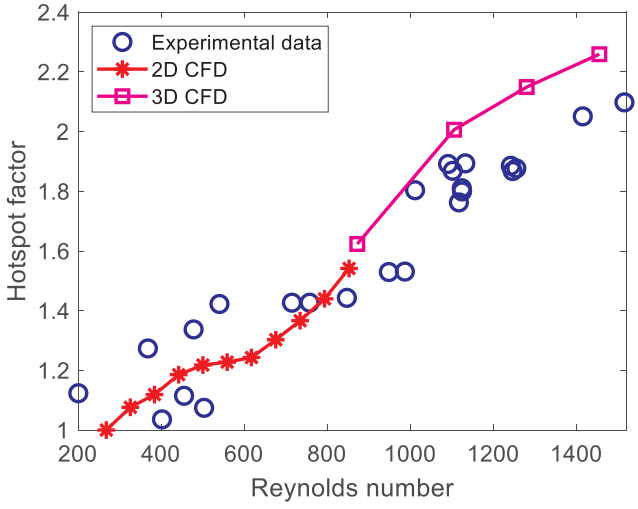

Fig. 16. Comparison of hotspot factors from experimental tests and 2D and 3D CFD simulations.

4.2. Dimensionless temperature distribution

The dimensionless temperature distribution is also found to be mainly controlled by *Re* [4]. Therefore, the dimensionless plate maximum temperatures (the higher of the two measured temperatures in each plate) against plate number and *Re* for all the experimentally tested cases are shown in Fig. 14. The kink at the bottom of pass 2 shown in the red box was due to a geometric deviation in the winding test rig that caused a persistent temperature disturbance. The overall temperature distribution gets more and more uneven with higher temperature shifting to the bottom part of the pass as *Re* increases. The dimensionless temperature distributions correspond to the flow distributions in Fig. 12.

CFD simulations of the 3-pass winding model with the mineral oil, P_{loss} = 2010 W/m^2, T_{in} = 60 °C and V_{in} ranging from 0.05 m/s to 0.4 m/s were conducted. The Reynolds numbers ranges from 268 to 1455. Since 2D CFD temperature results are not representative for reverse flow scenarios and reverse flows occur when *Re* is larger than approximately 1000, 11 cases with $Re < 860$ are simulated by 2D CFD and 4 more cases with *Re* of 872, 1105, 1280 and 1455 are simulated by 3D CFD. The dimensionless plate maximum temperatures (maximum of the two temperatures at the measured locations on the plate) from CFD

simulations are shown in Fig. 15.

For all the experimental tests the average winding to average oil temperature gradient ranged from 6.2 K at the highest flow rate (highest *Re*) to 12.7 K at the highest power loss. The average winding to average oil temperature gradient from the 2D and 3D CFD flow sweep ranged from 8.2 K at an inlet velocity of 0.4 m/s, to 14.1 K at an inlet velocity of 0.05 m/s. The temperature measurement uncertainty was ±1 °C, implying a worst-case plate maximum temperature to top oil temperature gradient uncertainty of ± 2K. Therefore, the dimensionless temperature uncertainty from the experimental tests ranged from ± 0.16 to ± 0.32. In addition, geometric deviations can contribute to the uncertainty. For example, the maximum dimensionless temperature discrepancy between experiment and CFD results (shown circled in Fig. 14 and Fig. 15) has a value of 0.5 and exists at plate 2 when *Re* is the highest. The average winding to average oil temperature gradient in the test was 6.2 K, meaning the actual temperature gradient was around 3 K. So considering that measurement uncertainty and geometric deviation can both contribute to this discrepancy, in general, it can be concluded that the dimensionless temperatures in Fig. 15 compare well with the experimental results shown in Fig. 14.

The maximum dimensionless temperature of each case is the hotspot factor; this can be extracted from Fig. 14 and Fig. 15. The comparison of the hotspot factors from the tests and the CFD simulations are shown in Fig. 16. The hotspot factor increases with the increase of *Re* due to increasingly more uneven flow distribution. The CFD results share the same trend with the measured data with maximum deviation being approximately 0.2, which corresponds to a maximum temperature difference being less than 3 °C.

5. Conclusion

Liquid flow and temperature distributions for liquid forced and directed (OD) cooling modes in a winding model have been investigated experimentally with different liquid inlet velocities, pass 1 inlet temperatures, plate power injections and liquid types. From dimensional analysis, the liquid flow and temperature distribution trends are found to be mainly controlled by the Reynolds number (*Re*) at the pass inlet. The higher *Re*, i.e. higher flow rate or lower viscosity, the more uneven the flow and temperature distributions would be.

Flow stagnation and reverse flows at high *Re* have been demonstrated by CFD simulations and PIV measurements together with a rise in hotspot temperature with increased flows under certain conditions; this is not predicted by conventional calculation methods.

Comparisons of liquid flow and temperature distributions are made between experimental tests and CFD simulations. When there are no reverse flows, 2D CFD results match well with the test results, indicating quasi-2D fluid flow and heat transfer processes. When reverse flows occur, 2D CFD temperature results are much higher than experimental results, while 3D CFD results are close to the experimental results. However average duct flow rate results from both 2D and 3D CFD match well with PIV measurements. With reverse flows, strong flow swirls exist at the entrance of the flow-reversed duct, close to the side walls, and part of the fluid flow escapes the closed loop and allows convection in the flow reversed ducts. Therefore, when reverse flows occur, 2D CFD temperature results are not reliable and 3D CFD modelling is needed.

The liquid flow and temperature distributions of all the experimentally tested cases are presented in their dimensionless forms and compared with their CFD counterparts. Flow fraction variations with *Re* from PIV measurements match well with results from correlations derived from 2D isothermal CFD simulations. The CFD dimensionless temperatures and hotspot factors match well with the test results, provided that 3D CFD is used where reverse flows occur.

Declaration of Competing Interest

The authors declare that they have no known competing financial interests or personal relationships that could have appeared to influence the work reported in this paper.

Acknowledgement

The authors would like to express their gratitude to M&I Materials, National Grid, Scottish Power, Shell Global Solutions, TJ|H2b Analytical Services, UK Power Networks and Weidmann Electrical Technology for their financial and technical contributions to the Transformer Research Consortium at The University of Manchester.

Appendix A. Supplementary material

Supplementary data to this article can be found online at https://doi.org/10.1016/j.applthermaleng.2019.114653.

References

[1] IEC standard 60076-7, Loading guide for oil-immersed power transformers, 2018.
[2] P. Jarman, X. Zhang, M. Daghrah, Q. Liu, Z. Wang, P. Dyer, A. Gyore, P. Smith, P. Mavrommatis, M. Negro, D. Walker, Uneven liquid flow distribution in radial ducts in transformer winding cooling systems shown by CFD and experimental measurements, Presented at the CIGRE Paris Session 2018, Paris, France, (2018).
[3] IEC standard 60076-2, Temperature rise for liquid-immersed transformers, 2011.
[4] X. Zhang, Z.D. Wang, Q. Liu, Interpretation of hot spot factor for transformers in OD cooling modes, IEEE Trans. Power Delivery 33 (3) (2017) 1071–1080.
[5] X. Zhang, Z. Wang, Q. Liu, P. Jarman, M. Negro, Numerical investigation of oil flow and temperature distributions for ON transformer windings, Appl. Therm. Eng. 130 (2018) 1–9.
[6] X. Zhang, Z. Wang, Q. Liu, Prediction of pressure drop and flow distribution in disc type transformer windings in an OD cooling mode, IEEE Trans. Power Delivery 32 (4) (2017) 1655–1664.
[7] A.J. Oliver, Estimation of transformer winding temperatures and coolant flows using a general network method, Generat., Trans. Distribut., IEE Proc. C 127 (6) (1980) 395–405.
[8] E. Rahimpour, M. Barati, M. Schäfer, An investigation of parameters affecting the temperature rise in windings with zigzag cooling flow path, Appl. Therm. Eng. 27 (11) (2007) 1923–1930.
[9] F. Torriano, M. Chaaban, P. Picher, Numerical study of parameters affecting the temperature distribution in a disc-type transformer winding, Appl. Therm. Eng. 30 (14) (2010) 2034–2044.
[10] H. Campelo, M. Quintela, F. Torriano, P. Labbé, P. Picher, Numerical thermofluid analysis of a power transformer disc-type winding, Presented at the IEEE Electrical Insulation Conference (EIC), Montreal, 2016.
[11] F. Torriano, H. Campelo, M. Quintela, P. Labbé, P. Picher, Numerical and experimental thermofluid investigation of different disc-type power transformer winding arrangements, Int. J. Heat Fluid Flow 69 (2018) 62–72.
[12] S. Tenbohlen, N. Schmidt, C. Breuer, S. Khandan, R. Lebreton, Investigation of thermal behavior of an oil-directed cooled transformer winding, IEEE Trans. Power Delivery 33 (3) (2018) 1091–1098.
[13] F. Torriano, P. Picher, M. Chaaban, Numerical investigation of 3D flow and thermal effects in a disc-type transformer winding, Appl. Therm. Eng. 40 (2012) 121–131.
[14] P. Allen, O. Szpiro, E. Campero, Thermal analysis of power transformer windings, Electric Mach. Electromech. 6 (1) (1981) 1–11.
[15] J.-M. Mufuta, Comparison of experimental values and numerical simulation on a set-up simulating the cross-section of a disc-type transformer, Int. J. Therm. Sci. 38 (5) (1999) 424–435.
[16] M. Yamaguchi, T. Kumasaka, Y. Inui, S. Ono, The flow rate in a self-cooled transformer, Power Apparatus and Systems, IEEE Transactions on, vol. PAS-100, no. 3, 1981, pp. 956–963.
[17] M. Nakadate, K. Toda, K. Sato, D. Biswas, C. Nakagawa, T. Yanari, Gas cooling performance in disc winding of large-capacity gas-insulated transformer, IEEE Trans. Power Delivery 11 (2) (1996) 903–908.
[18] X. Zhang, M. Daghrah, Z.D. Wang, Q. Liu, P. Jarman, M. Negro, Experimental verification of dimensional analysis results on flow distribution and pressure drop for disc type windings in OD cooling modes, IEEE Trans. Power Delivery 33 (4) (2018) 1647–1656.
[19] M. Daghrah, Z. Wang, Q. Liu, C. Krause, P. Smith, Characterization of oil flow within radial cooling ducts of disc type transformer windings using particle image velocimetry, IEEE Electr. Insul. Mag. 35 (2) (2019) 9–17.
[20] M. Daghrah, Z. Wang, Q. Liu, D. Walker, P. Smith, P. Mavrommatis, Design of experimenal setup to study factors affecting hot spot temperature in disc type winding transformers, Presented at the IET International Conference on Resilience of Transmission and Distribution Networks (RTDN), Birmingham, UK, (2015).
[21] X. Zhang, Z. Wang, Q. Liu, A. Gyore, K. Rapp, Investigation of the total flow rates in oil natural transformer retrofilling scenarios, *2019 IEEE 20th International*

Conference on Dielectric Liquids (ICDL), Rome, Italy, (2019).
[22] X. Zhang, Z.D. Wang, Q. Liu, M. Negro, A. Gyore, P.W.R. Smith, Numerical investigation of influences of liquid types on flow distribution and temperature distribution in disc type ON cooled transformers, 25th-29th June, Presented at the The 19th IEEE International Conference on Dielectric Liquids (ICDL), Manchester, UK, (2017).
[23] M. Daghrah, Z.D. Wang, Q. Liu, C. Krause, P. Dyer, P. Jarman, Influence of winding geometrical deviations on the hot spot temperature in a disc type power transformer, Presented at the 20th International Symposium on High Voltage Engineering (ISH), Buenos Aires, Argentina, (2017).
[24] M. Daghrah, Z. Wang, Q. Liu, A. Hilker, A. Gyore, Experimental study of the influence of different liquids on the transformer cooling performance, IEEE Trans. Power Delivery 34 (2) (2019) 588–595.